JOURNAL OF PROPULSION AND POWER
Vol. 19, No. 4, July–August 2003

Rotordynamic Bearing Dampers for Cryogenic Rocket Engine Turbopumps

Bugra H. Ertas*
Texas A&M University, College Station, Texas 77840
Eyad Al-Khateeb†
Aramco, 31311 Dhahran, Saudi Arabia
and
John M. Vance‡
Texas A&M University, College Station, Texas 77843

It is a common practice for cryogenic turbomachines to utilize stiffly mounted bearings due to the incapability of providing significant damping with conventional methods and designs. With no damping available, the historical motive behind this design practice was to elevate all critical speeds above the maximum running speed. The desire for higher energy density has raised the running speeds of rocket engine turbopumps very near, or even above, the first three critical speeds. A companion paper gives experimental evidence that accurate prediction of these critical speeds with the turbopump rotor on ball bearings with stiff supports is not practically possible. The feasibility of applying a metal mesh damper with soft supports in a cryogenic engine is investigated. To date the focus has been on cryogenic experimental tests, rotordynamic simulations, and possible bearing support design schemes to justify the incorporation of a metal mesh bearing support in a liquid rocket engine fuel turbopump. Success of the design is dependent on the amount of damping that the damper retains at cryogenic temperatures and its ultimate effect on fuel turbopump rotordynamics, especially subsynchronous instability.

Nomenclature

C	=	equivalent viscous damping coefficient
F	=	force amplitude
f_0	=	force
h	=	hysteretic damping coefficient
k	=	stiffness coefficient
m	=	modal mass
t	=	time
X	=	vibration amplitude
x	=	displacement
x'	=	velocity
x''	=	acceleration
μ	=	structural damping loss factor
ω	=	vibration frequency

I. Introduction

PAST research on metal mesh damping at the Turbomachinery Laboratory has shown that metal mesh donuts can be used as an effective vibration damper for turbomachines. Zarzour and Vance[1] tested steel wire mesh for a range of interference fits, for high operating temperatures, and in lubricated conditions. Their results indicated that metal mesh could be used in aircraft gas turbine engines as a substitute for squeeze film dampers. Further testing of metal mesh, conducted by Al-Khateeb and Vance,[2] also confirmed the presence of useful amounts of damping for both stainless-steel wire mesh and copper wire mesh. They investigated the behavior of the metal mesh element in parallel with a squirrel cage, which enabled them to develop a refined hysteretic model for the damper. Although this research revealed significant amounts of damping, the effects of low temperatures were unknown.

A possible application of the metal mesh damper elements in liquid fuel rocket engines depends on the amount of damping retained at cryogenic temperatures and the overall impact on turbopump rotordynamics. Past research for applying metal mesh to the bearing supports in cryogenic rocket engines is limited. The authors found two references that addressed the option of using soft bearing supports in conjunction with wire mesh. Childs[3] reports bench tests performed on metal mesh in efforts to solve rotordynamic stability problems in the space shuttle main engine fuel turbopump. Childs's 1978 analysis of the space shuttle turbopump rotordynamics indicated superior turbopump operation with asymmetric soft supports and metal mesh when compared to all other rotor-bearing design considerations. A management decision was made to use hard supports instead.

Metal mesh dampers were used to solve subsynchronous instability problems and high synchronous vibration amplitudes for the LE-7 Liquid Hydrogen Turbopump.[4] From Okayasu et al.,[4] "In the early design, the stiff bearing support was used and so several vibration problems occurred." The addition of the so called friction dampers in the bearing supports of the LE-7 enabled the machine to operate above the third critical speed at 46,130 rpm. Their results for the metal mesh wire donuts showed that the damping factor decreases with amplitude so that the optimum value from a small-amplitude test must be made larger for best performance through the critical speeds. They also reported that the metal mesh showed the most effective source of damping compared to other damping components, such as the grooved damper seals used between first- and second-stage pump impellers.

The objective of the present work is to investigate the feasibility of incorporating two metal mesh damper elements into a liquid hydrogen turbopump. Three main topics are presented: 1) experimental tests consisting of cryogenic cooling of metal mesh samples and measuring rotordynamic coefficients, 2) turbopump design, which

Received 21 January 2002; presented as Paper 2002-4160 at the AIAA/ASME/SAE/ASEE 38th Joint Propulsion Conference and Exhibit, Indianapolis, IN, 7–10 July 2002; revision received 20 January 2003; accepted for publication 18 February 2003.

*Research Assistant, Turbomachinery Laboratory, Test Cell Number 136, Farm & Market Road 2818 and George Bush Drive: also Project Engineer at Bearings Plus/KMC Bearings, 8525 Monroe, Houston, TX, 77061; bugra_e@yahoo.com. Student Member AIAA.

†Rotating Equipment Engineer, P.O. Box 5000; eyad.khateeb@aramco.com.

‡Professor, Mechanical Engineering Department, Mail Stop 3123; jvance@mengr.tamu.edu.

suggests a design scheme for incorporating a metal mesh/squirrel cage bearing support system, and 3) turbopump rotordynamic simulations for stiffly mounted bearings and for softly mounted bearings with metal mesh damping.

II. Experimental Setup

Two different types of testing were conducted on the metal mesh donut samples: 1) ambient temperature forced excitation tests and 2) cryogenic forced excitation tests. In both cases the excitation was from a shaker. Six individual metal mesh donuts were tested in ambient (17°C) and cryogenic (to −190°C) temperatures. The dimensional and material data for the samples is shown in Table 1. Because of the variation in surface features of the donuts, dimensions shown in Table 1 were averaged from three measurements taken at different circumferential locations. The percent density of the samples represents the ratio of actual weight to the theoretical weight if the donuts were solid. The experiments to determine stiffness and damping involved varying three parameters: 1) metal mesh temperature, 2) excitation amplitude, and 3) magnitude of interference fit between the metal mesh and collar. The temperature of the mesh was lowered using liquid nitrogen, which has a temperature of −195.8°C. Excitation amplitudes during vibration tests ranged from 0.0762 mm (3 mils) to 0.1524 mm (6 mils) peak to peak. Collars or rings were used to control the interference fit during testing. Inner diameters of the rings varied from 91.44 mm (3.600 in.) to 94.74 mm (3.730 in.), and the average mass of the collars were measured to be 0.908 kg (2.00 lb).

A. Preliminary Ambient Shaker Tests

During cryogenic testing, the metal mesh samples were exposed to extremely low temperatures, which can have unfavorable effects on force and displacement transducers. The low temperatures required that the force transducer to be at a safe distance from the liquid nitrogen and metal mesh sample. Two different configurations for the transducers were used. First, the force transducer was mounted directly to the collar, and shaker tests were conducted to determine the stiffness and damping. Next, the force transducer was mounted farther from the collar (using a stinger rod), which would be the same mounting to be used with the cryogenic hardware. The effect of the stinger rod between the transducer and the collar was initially unknown; therefore, stiffness and damping coefficients for the two configurations were compared. It was found that there was no significant difference between the metal mesh stiffness and damping for the two configurations, in the frequency range of interest.

B. Cryogenic Forced Excitation Testing

The experimental setup used for the cryogenic shaker tests is shown in Fig. 1. Because of the low-temperature environment in the cryogenic chamber, both transducers were located outside the chamber. For these tests, the proximity probe monitored the vibration from a stinger on the opposite side of the collar that was in line with the force transducer stinger. Liquid nitrogen entered the chamber from the top and also exited from the top to a vent. In efforts to maintain the lowest temperature possible, two layers of thermal insulation were used. The first layer of insulation was fiberglass fabric, and the outer layer of insulation was silver Mylar®. Metal mesh temperatures were monitored during the experiments with a cryogenic thermocouple. During initial testing the stingers reached temperatures below freezing, therefore inducing the collection of frost between the stinger and chamber housing clearance. To avoid this complexity, a plexiglass housing was constructed to purge all moisture using dry nitrogen gas. This feature prevented ice and frost from forming within the stinger/housing clearance. Another concern with the cold stinger was the effects on the transducers. The force transducer was calibrated to only −71°C, and so a hairdryer was directed onto the force transducer to keep the temperature above 0°C (no ice forming). A similar problem with the proximity probe was that the end of the stinger formed ice, and it also had significant shrinkage during testing (monitored with the voltmeter). Therefore, another hairdryer was used in this location to counteract ice forming and material shrinkage.

The instrumentation setup used for the cryogenic testing is shown in Fig. 2. Excitation amplitudes of the collar were controlled with the shaker amplifier. Maximum amplitudes were 0.1524 mm (6 mils) peak to peak and were monitored by using an oscilloscope. Although other options were investigated, the excitation signal to the shaker

Table 1 Metal mesh donut samples

Mesh	Material	% Density	Mass, kg	Inner diameter, mm	Outer diameter, mm	Width, mm
1	Steel mesh	41	0.181	68.58	94.2594	10.6172
2	Steel mesh	41	0.185	68.58	94.2594	10.8966
3	Steel mesh	22	0.102	68.58	95.0214	10.9728
4	Steel mesh	22	0.101	68.58	94.9198	10.9982
5	Copper mesh	26	0.171	68.58	93.2942	10.8204
6	Copper mesh	26	0.117	68.58	93.1672	10.668

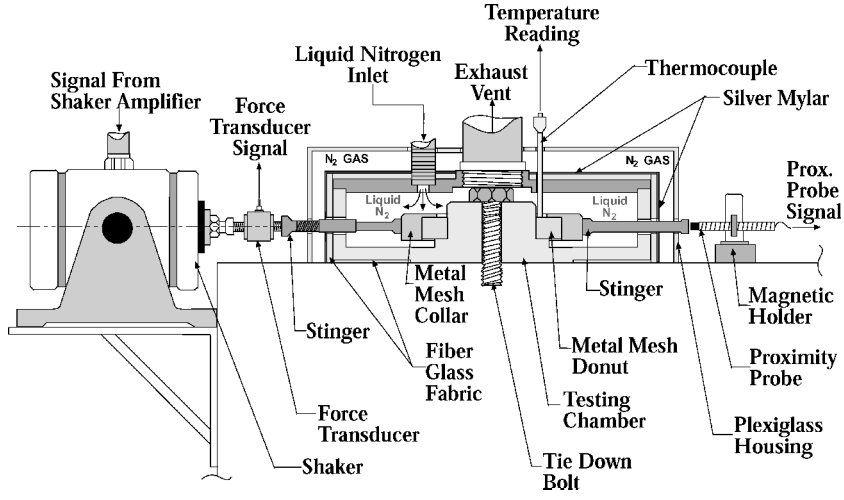

Fig. 1 Cryogenic shaker test setup.

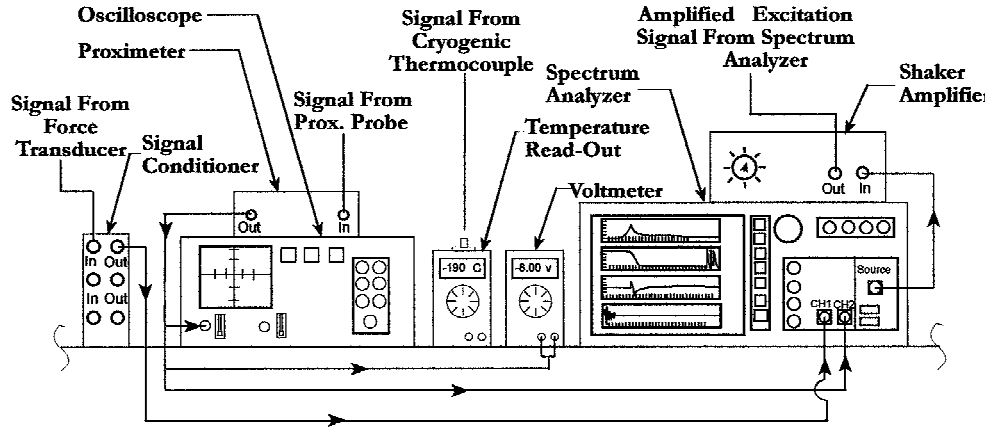

Fig. 2 Instrumentation setup.

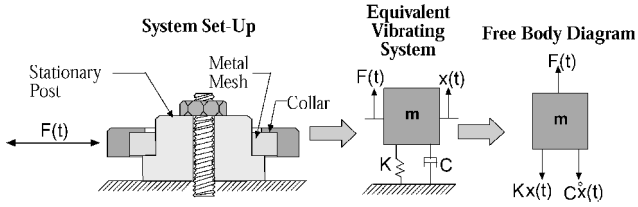

Fig. 3 SDOF system model.

was a periodic chirp with a frequency range of 0–400 Hz. The signals from the transducers were ultimately recorded and processed with a Hewlett–Packard signal analyzer. Five different traces were saved in the analyzer: 1) receptance (X/F), 2) phase, 3) imaginary part of the receptance, 4) real part of the receptance, 5) coherence, and 6) both force and displacement time traces. The five traces were used to determine stiffness and damping coefficient for the donuts.

The experimental procedure was divided into two main tests: 1) ambient tests just before conducting the cryogenic testing and 2) cryogenic testing with liquid nitrogen. Testing was conducted in this fashion in efforts to maintain a controlled experiment and set-up. The first step for the cryogenic testing was to initiate liquid nitrogen flow into the chamber. Second, the hair dryers were started and the temperature was monitored until reaching a desired value. The temperature was decreased to approximately -180°C to -190°C. After reaching the desired temperature, nitrogen flow ceased, and data collection started with the analyzer. The experimental setup and procedure was proven to be inexpensive, efficient, and effective.

III. Theoretical Approach

The vibration response of the metal mesh/collar assembly, shown in Fig. 3, can be modeled as a single-degree-of-freedom (SDOF) system with an effective modal mass, a system damping, and a modal stiffness. Assuming linear spring and damper elements, the SDOF model of the metal mesh/collar assembly can be expressed with the following second-order differential equation:

$$x''m + x'c + xk = f_0 \tag{1}$$

where C is the system damping and k is the stiffness. When it is assumed that $x = Xe^{i\omega t}$ and $f_0 = Fe^{i\omega t}$ and derivatives are taken, Eq. (1) becomes

$$-mX\omega^2 e^{i\omega t} + cXi\omega e^{i\omega t} + kXe^{i\omega t} = Fe^{i\omega t} \tag{2}$$

Dividing Eq. (2) by $Xe^{i\omega t}$, the equation becomes

$$X/F = 1/(k - m\omega^2 + ic\omega) \tag{3}$$

where X/F is the desired transfer function. The inverse has an imaginary $(i\omega c)$ and real part $(k - m\omega^2)$. Next, when the absolute value of the transfer function Eq. (4) is taken, the function can be graphed. An example receptance function from the experiments is shown in Fig. 4. Thus,

$$|X/F| = 1\Big/\sqrt{(k - m\omega^2)^2 + (c\omega)^2} \tag{4}$$

Figure 4 shows that the vibration frequency was changed from ~100 to ~150 Hz when subjected to cryogenic temperatures. The damping of the system dictates the bandwidth of the peak and the peak height of the transfer function. As the damping is reduced the peak response of the transfer function is increased and the bandwidth is reduced. The stiffness controls the amplitude of the left side of the function and changes the horizontal position of the peak. Varying the mass changes the curvature of the right side of the function.

The damping and stiffness coefficients of the metal mesh damper donuts were found by performing a curve fit of the (X/F) transfer function (amplitude, phase, real part, and imaginary part) computed by the dynamic analyzer from the measured data. The transfer function data were collected from shaker tests on each metal mesh damping element, at both ambient and cryogenic temperatures.

Because of the dependency of metal mesh stiffness and damping coefficients on vibration amplitude, the maximum amplitude (when passing through the natural frequency) was maintained at about 6 mils (0.1524 mm) peak to peak for all tests (except for amplitude-dependency tests). This amplitude was chosen because it is representative of the target maximum critical speed amplitude at the bearings. Operating at a lower amplitude results in higher damping and stiffness from the metal mesh elements, provided that all other conditions remain the same. Maintaining constant maximum amplitude in the tests omits the effect of amplitude from one testing condition to another. The data were then analyzed to extract the equivalent linear stiffness and viscous damping coefficients of the metal mesh element.

A MathCAD code was used to extract the stiffness and damping coefficients from the transfer function data in the half-power frequency range. Three parameter identification methods are used in the code: 90-deg phase, nonlinear regression, and minimums of the real and imaginary parts. The reported stiffness and damping coefficients were evaluated as the average calculated by these three methods. The uncertainties in measurements for the three different methods were similar. Therefore, averaging the results from all three methods yielded a larger pool of data to consider when determining damping and stiffness coefficients. The linear viscous damping coefficient was chosen to represent damping to facilitate its use in rotordynamic modeling software. Also, the imaginary part of the transfer function seems to agree better with a viscous model. The stiffness coefficient is calculated from the measured system mass and the natural frequency that was calculated in each method.

IV. Experimental Results

A. Results for Ambient Measurements at Different Interference Fits

Metal mesh samples were tested at different interference fit values to investigate the dependency of dynamic coefficients on interference. All tests showed an increase, in both stiffness and damping,

with interference. Results from these tests are shown in Table 2. Sample 2 (high-density steel mesh) was tested ambient at four different interference levels. Figures 5 and 6 show the stiffness and damping, respectively, plotted against interference values.

Results from ambient tests of samples 2, 4, and 6 are shown in Figs. 5 and 6, representing the three types of samples received (high-density steel, low-density steel, and low-density copper). For both stiffness and damping, we can observe a linearly proportional relationship with interference. This is very useful in determining the required interference to achieve a certain value of damping or stiffness.

Table 2 Results[a] from ambient measurements at different interference fits

Metal mesh	Interference, mm	Direct stiffness, kN/m	Direct damping, N · s/m
Sample 1,	0.2286	1263	744
41% density	0.3302	1359	750
steel	0.4318	1657	872
Sample 2,	−0.0508 (clearance)	650	382
41% density	0.0508	1189	529
steel	0.4572	2414	729
	0.6604	3064	989
Sample 3,	0.2794	2014	653
22% density	0.3810	1486	648
steel	0.5334	2492	672
Sample 4,	0.1778	1064	434
22% density	0.2794	1452	660
steel	0.4318	2056	660
Sample 5,	0.3302	571	317
26% density	0.4318	663	464
copper	0.5842	1108	662
Sample 6,	0.2032	463	364
26% density	0.3048	741	492
copper	0.4572	1062	539
	0.5588	1434	593

[a]Uncertainty ±2.5%.

B. Results for Ambient/Cryogenic Measurements

Table 3 provides a comparison of results for tests at ambient and cryogenic temperatures. Metal mesh element 1 (high-density steel) could not be tested at cryogenic temperatures at 6-mil peak to peak amplitude due to the output force limit of the shaker. When the low-density copper sample 6 was tested with its high interference ring, a 6-mil peak to peak vibration level was barely reached at cryogenic temperatures.

The behavior of metal mesh coefficients at low temperature was somewhat surprising, especially damping. The stiffness increased significantly for all samples, which is expected due to material stiffening at low temperature in addition to the effect of increased interference. This increase in stiffness, however, will not significantly affect rotordynamic behavior because the squirrel cage would provide most of the support stiffness.

Damping, on the other hand, remained almost unchanged for the steel mesh samples, but increased significantly for the copper mesh samples. This behavior was confirmed in the cryogenic testing of sample 6 at high interference, which gave the highest damping value even though it had the lowest average testing temperature of −190°C.

V. Turbopump Bearing Support Designs

Preliminary design studies for the liquid hydrogen turbopump shown in Fig. 7 concluded that toroidal-shaped metal mesh bearing supports (donuts) could have the following maximum dimensions for both the pump end and turbine end bearings: 68.58 mm i.d. × 91.4 mm o.d. × 12.1 mm L (axial). Figure 7 shows two different bearing support mounting configurations. The bearing supports above the horizontal split line represent the existing hard- or stiffly

Table 3 Cryogenic/Ambient test results[a]

	Ambient temp. results (∼15°C)			Cryogenic temp. results			Percent change, %	
Metal mesh sample	Interference, mm	K, kN/m	C, N · s/m	Temp, °C	K, kN/m	C, N · s/m	ΔK	ΔC
Steel 2, 41% density	0.0508	1,189	529	−175	1,675	506	41	−4
Steel 3, 22% density	0.3810	1,486	648	−170	3,203	669	135	6
Steel 4, 22% density	0.2794	1,452	660	−165	3,144	585	116	−11
Copper 5, 26% density	0.4318	663	464	−180	944	592	50	28
Copper 6, 26% density	0.3048	741	492	−190	1,184	620	60	26

[a]Uncertainty ±2.5%.

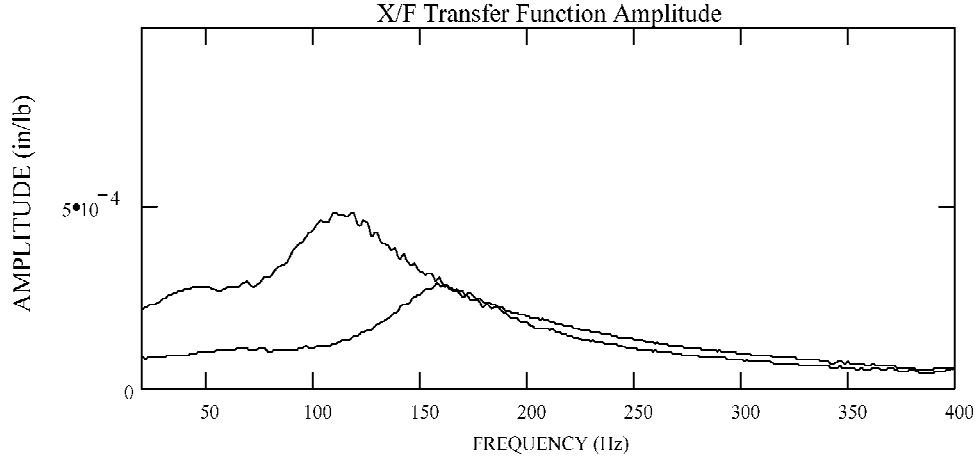

Fig. 4 Transfer function: ——, ambient and ——, cryogenic.

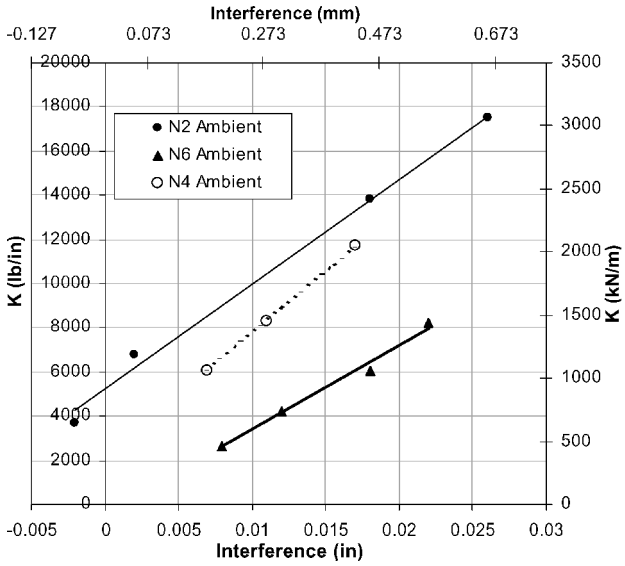

Fig. 5 Stiffness variation with interference at ambient temperature.

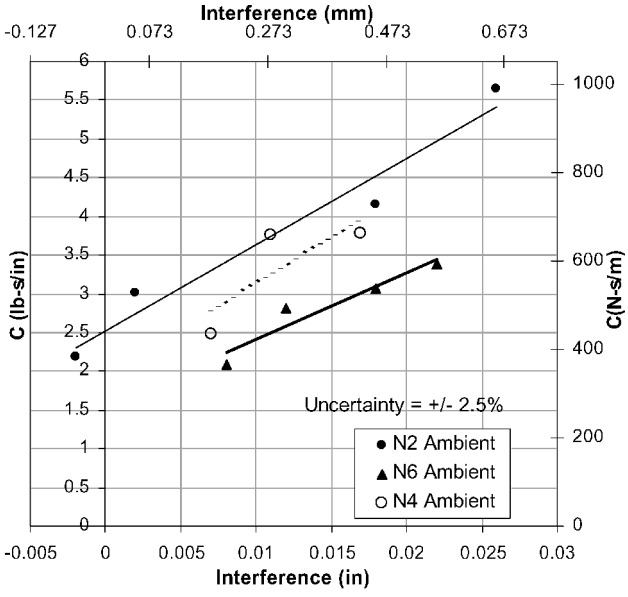

Fig. 6 Damping variation with interference at ambient temperature.

mounted ball bearings, and the bearing supports below the horizontal split line are designs for soft-mounted ball bearings. A rotor-bearing system is hard mounted when the bearing support stiffness is high enough to generate significant rotor bending. The term soft mounted is used to describe a rotor-bearing system in which all of the eigenvectors are rigid-body modes. Closeup views of the bearing supports are shown in Fig. 8.

The existing turbopump design utilizes hard-mounted angular contact ball bearings, one at the pump end and one at the turbine end. The pressure balance across the first and second pump stages is controlled by the interstage pressure balance seal, and the axial thrust is transmitted through the bearings to the pump-end bearing carrier. The pump-end bearing is fixed, and the turbine-end bearing is allowed to float axially by the use of an axial preload spring. With the existing design, the radial stiffness at the bearing locations is strongly dependent on the radial stiffness of the ball-bearings (due to the stiff bearing supports), and the radial ball-bearing stiffness is dictated by the axial thrust. Based on past research on the ball bearing in Fig. 8 at the Turbomachinery Laboratory,[5,6] the radial stiffness varies an order of a magnitude depending on the axial thrust, dynamic radial loading, and misalignment. The fact that the axial thrust loading in the machine ranges between 0 and 4448 N makes the critical speed locations difficult to predict. The radial stiffness can also affect the onset speed of instability of the machine, which would also vary within a range (possibly in operating range). The use of the metal mesh/squirrel cage cartridges will render the radial ball-bearing stiffness irrelevant and will also provide damping at the bearing supports.

The addition of soft supports will reduce critical speeds (therefore, reducing peak amplitudes), increase effective damping (therefore, increasing stability and reducing synchronous response), and will transform the bending modes generated by the existing hard mounts to rigid-body modes. A major factor considered when designing for the radial stiffness of the squirrel cage supports was the radial gear load generated from the liquid oxygen pump. Lateral in-flight maneuver loads for these particular rocket engines are insignificant compared to the gear load; therefore, maneuver loads were not considered. To incorporate metal mesh into the pump design, it was required that the metal mesh be mounted in parallel with a squirrel cage. The design scheme for incorporating the metal mesh and squirrel cage is shown in Figs. 7 and 8. The functions of the pump-end squirrel cage are as follows: 1) to support axial thrust through the ribs of the cage, 2) to provide radial compliance to the rotor-bearing system, independent of axial thrust load variations, 3) to allow concentric operation between the bearing outer race and fuel pump housing, 4) to maintain the interstage pressure balance system, and 5) to provide containment for all of the metal wire mesh. The wire containment and pressure sealing system is

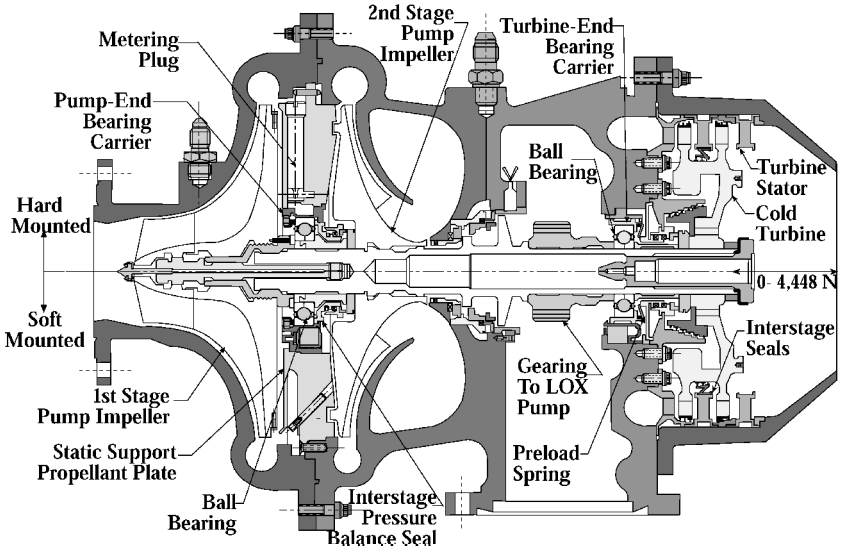

Fig. 7 Liquid hydrogen fuel turbopump.

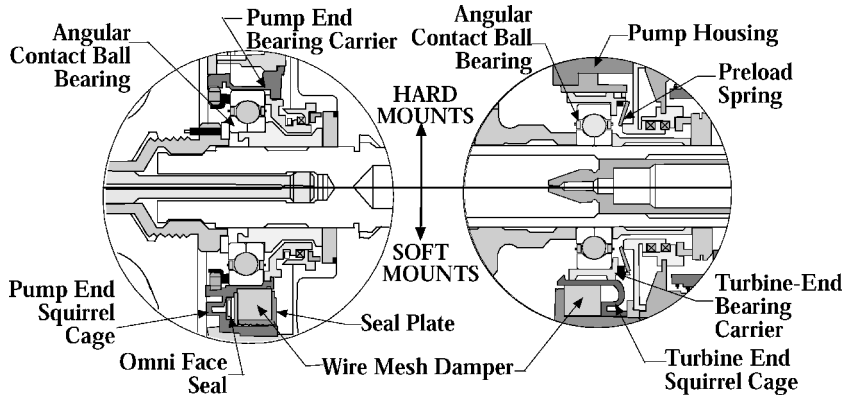

a) Pump end b) Turbine end

Fig. 8 Turbopump bearing support designs.

composed of five components. Pressure from the second stage and first stage is restricted through the cage by the use of face seals and a seal plate. The majority of the pressure-induced loading is supported by the seal plate, which is screwed into the outer rim of the squirrel cage. A finite element analysis of the seal plate to verify structural integrity for a 600-psi pressure loading was performed, and then the seal plate design was optimized to have low stresses and deflections. The cover plate was designed to contain the metal mesh wires by designing the clearance to the inner squirrel cage rim to be less than the nominal wire diameter of the metal mesh.

An important factor considered when designing the pump-end squirrel cage was the requirement to maintain the interstage pressure balance system across the first- and second-stage pump impellers. The pressure balance system is necessary to limit axial loading to a maximum of 4448 N. The current design bleeds high pressure from the second stage to the first stage (behind the first-stage impeller) by the use of controlled flow through an orifice. The design with the metal mesh dampers at the pump end has accounted for the pressure bleed system requirements.

The turbine-end squirrel cage has many of the same functions as the pump-end squirrel cage. The turbine-end squirrel cage is required to 1) provide radial compliance to the rotor bearing system, independent of axial load variations, 2) to enable concentric operation between the bearing carrier and pump housing, and 3) to act as a containment unit for the metal mesh wires.

VI. Turbopump Rotordynamics

A. Force Coefficients of the Metal Mesh Bearing Supports

The test data from the copper mesh donuts measured at cryogenic temperatures (−190°C) in the Texas A&M Turbomachinery Laboratory (TL) were used as input to the computer code XLROTOR to determine response to unbalance, critical speeds, mode shapes, and stability characteristics of the liquid hydrogen turbopump rotor in Fig. 7. It is shown later that the metal mesh damping, in combination with a low stiffness squirrel cage, is very beneficial to its rotordynamic performance. The total radial stiffness of the bearing support can be varied by varying the thickness of the squirrel cage ribs. A value of 6130 kN/m was assigned to the combined radial support stiffness for both the pump end and turbine end. Experiments in the TL have shown that installing the mesh in a squirrel cage has no measurable effect on the hysteretic damping coefficient.[2]

To incorporate the metal mesh damping into XLROTOR, it was required that the hysteretic damping measured in the experiments be transformed to an equivalent viscous damping value. Table 4 shows the frequency-dependent equivalent viscous damping provided by the metal mesh. The equivalent damping C is a function of vibration frequency and can be obtained by dividing the hysteretic damping coefficient h by the vibration frequency ω. Another useful factor to define is the structural damping loss factor μ. The relationship between these factors is

$$C = (k \cdot \mu)/\omega = h/\omega \tag{5}$$

Table 4 Test data[a] converted to equivalent viscous damping[b]

O.D., mm	Stiffness, kN/m	Damping, N · s/m	Frequency, cycle/min	h, N/m
91.44	1,149	876.54	6,000	550.75
91.44	1,149	438.27	12,000	550.75
91.44	1,149	292.10	18,000	550.75
91.44	1,149	219.13	24,000	550.75
91.44	1,149	175.31	30,000	550.75
91.44	1,149	146.09	36,000	550.75
91.44	1,149	125.22	40,000	550.75

[a]Uncertainty ±2.5%.
[b]Copper wire mesh donut, 26% density, $E = 5{,}687$ kN/m^2, 68.58 mm I.D., 10.16 mm axial thickness. From cryogenic testing, June 2001, average $c = 578$ N · s/m.

B. Modeling the Fuel Pump Rotordynamics Without Metal Mesh

Vance used dimensional data scaled from a turbopump dimensional drawing to construct a "lookalike" computer model that has critical speed characteristics similar to those observed on the existing rocket engine. This model was used in the XLROTOR computer code to compare rotordynamic performance with bearings mounted on the existing stiff supports and then with the ball bearings mounted on metal mesh supports. A description of the results follows here.

The turbopump rotor is shown in Fig. 9, and Fig. 10 shows the computer generated rotor-bearing model. The bearing supports are shown to be at stations 5 and 11. Internal friction in the built-up rotor assembly is destabilizing and has been included. The friction loss coefficient used in the analysis was chosen to be 0.1 at each station. This value is typical of built-up rotors such as the turbopump rotor shown in Fig. 9. Unbalance was added to the pump end (0.028 oz·in.) and to the turbine end (0.065 oz · in.). These unbalance values were generated by offsetting the center of gravity of the corresponding station 0.0254 mm (0.001 in.). Figure 11 shows an eigenvector (mode shape) plot of a forward whirl mode with a frequency of 29,125 cycles/min computed at a shaft speed of 30,000 rpm. This mode is unstable as indicated by −0.392% of critical damping (zeta = −0.0039). It could be referred to as a turbine mode because the largest amplitude is at the turbine end, and it shows the shape of the critical speed at 30,000 rpm. This instability could be incorrectly interpreted in vibration measurements as a critical speed, but it is not related to unbalance.

Figure 11 shows another forward whirl mode at 36,538 cycles/min computed at a shaft speed of 36,600 rpm. The mode is also very slightly subsynchronous because the whirl frequency is just slightly

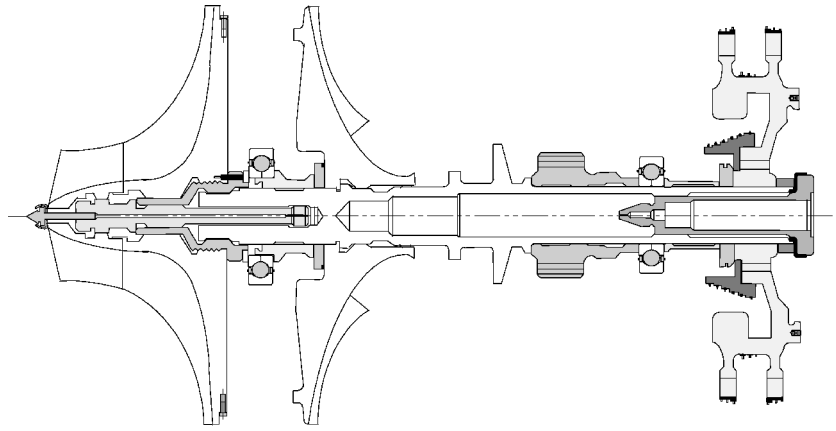

Fig. 9 Liquid hydrogen fuel turbopump rotating assembly.

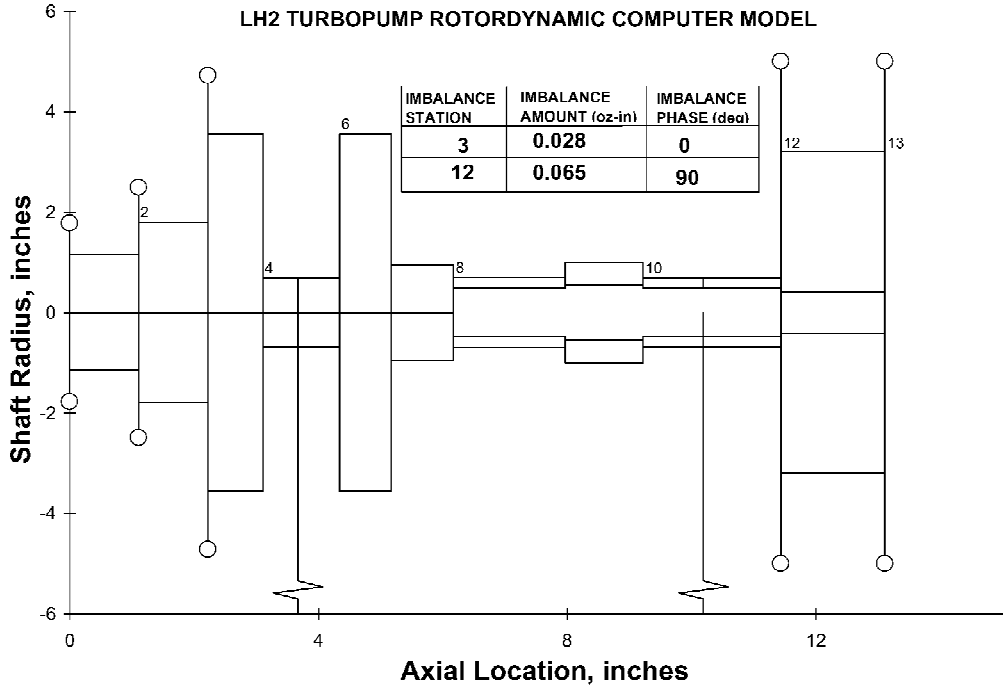

Fig. 10 Rotor-bearing computer model.

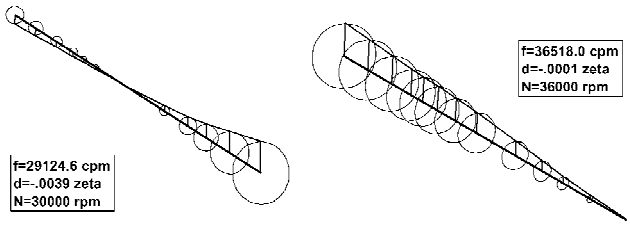

a) turbine end mode **b) pump end mode**

Fig. 11 Unstable modes for stiff bearing mounts (forward whirl); damped eigen value mode shape plots, hard supports (450 K · lb/in.), damping h = 943 lb/in.

lower than the shaft speed. The second vibration mode is also unstable (zeta = −0.0001) due to the internal friction and low bearing support damping. This mode could be referred to as a pump mode because the largest amplitude is at the pump end.

This type of rotordynamic instability is unaffected by rotor unbalance and is observed as a sudden increase (not a ramp) in vibration amplitude when the threshold speed of instability is reached. Note the bending of the rotor in both modes, which is what allows the internal friction to act. A major benefit of soft supports is to reduce this type of rotor bending in whirl modes and create rigid-body modes. Backward modes were also computed but are not presented here because they seldom produce critical speeds and are never unstable under the influence of internal friction.

Figure 12 shows the synchronous response to unbalance at the pump-end bearing. Notice the large amplitudes at the two critical speeds due to the small amount of damping in the system. Figure 13 shows the dynamic bearing loads, excited by rotor unbalance, at the pump-end bearing and turbine-end bearing. The dynamic loads reach destructive levels, exceeding 120 kN at the second critical speed. Figure 13 also shows that the dynamic loads are also high at the turbine-end bearing.

C. Rotordynamics with Metal Mesh Dampers

In Figs. 14–16 the same rotordynamic analysis was performed with a set of metal mesh bearing supports replacing the hard supports. All rotor parameters will be exactly the same as before. The first two forward eigenvalue mode shapes for the soft-mounted case are shown in Fig. 14. Note that the two highest frequency whirl modes of 9170 and 10,482 rpm are below the maximum operating speed and show no bending. Both eigenvalues are stable

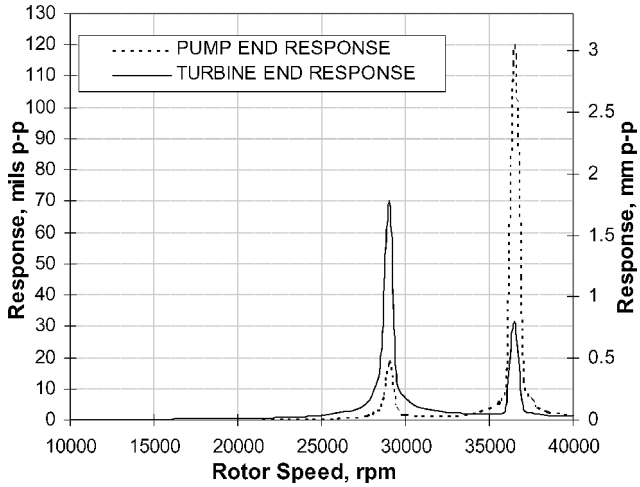

Fig. 12 Response to imbalance with hard mounts, 450 K · lb/in., and damping h = 943 lb/in.

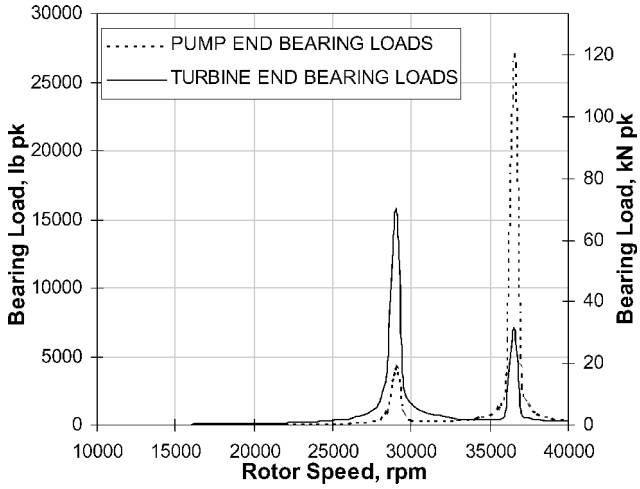

Fig. 13 Bearing loads with hard mounts, 450 K · lb/in., and damping h = 943 lb/in.

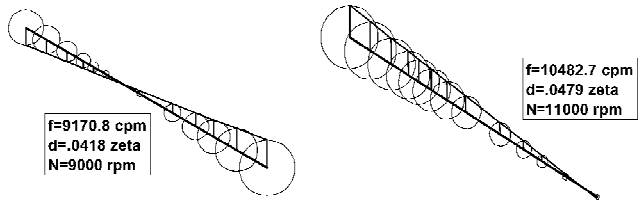

Fig. 14 First two forward whirl modes for soft supports with metal mesh; damped eigen value mode shape plots, metal mesh and squirrel cage supports; combined parallel support stiffness 35 K · lb/in.

with positive zeta values of 0.0148 and 0.0479. The response to unbalance for both bearings is shown in Fig. 15. Because of the damping available at the soft bearing supports, the vibration response shows a major decrease in amplitude by a factor of 40. Figure 16 shows a significant decrease in dynamic bearing loads after the bearing support modification. The dramatic change in rotordynamic behavior can be attributed to 1) soft supports, with lower stiffness and lower critical speeds, which produce lower rotating unbalance loads, and 2) direct damping at the bearing supports.

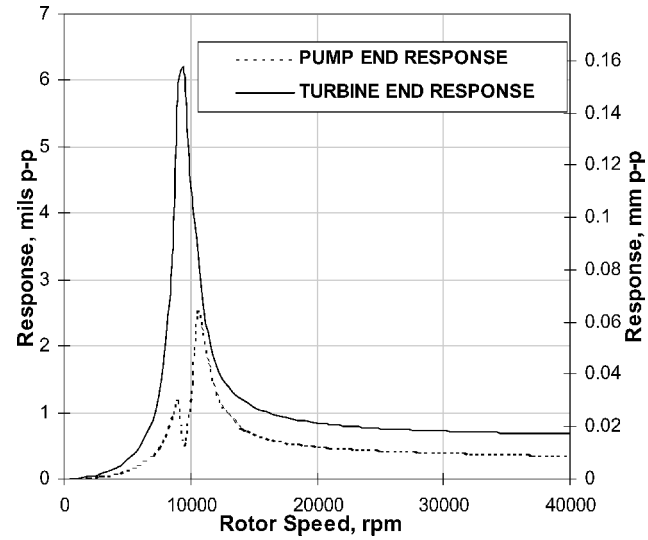

Fig. 15 Response to imbalance with soft mounts, metal mesh and squirrel cage supports.

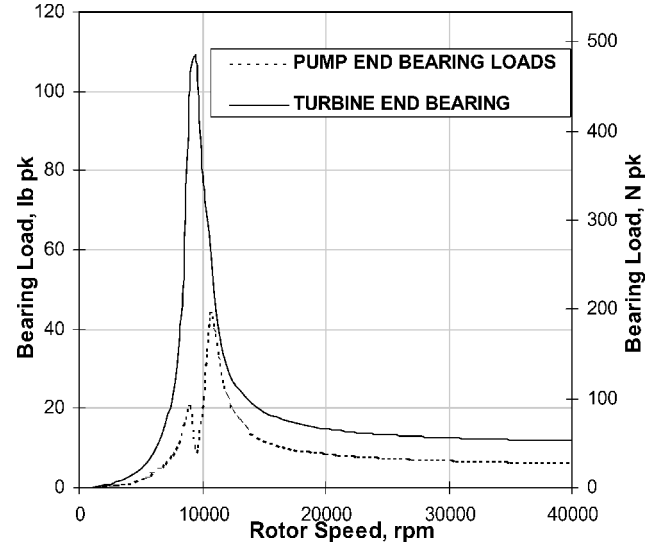

Fig. 16 Bearing loads for soft mounts, metal mesh and squirrel cage supports.

VII. Conclusions

This feasibility study has shown the likelihood of achieving the following improvements in rotordynamic performance of a liquid hydrogen fuel turbopump by mounting the bearings on metal mesh supports: 1) reduction of vibration amplitudes by a factor of 40 at the bearings, 2) reduction of dynamic loads at the bearings by several orders of magnitude, 3) removing critical speeds from the normal operating range of the turbopump, 4) reducing rotor bending in any potential subsynchronous whirl modes, and 5) stabilizing subsynchronous whirl modes that might otherwise be unstable from internal friction.

The performance of metal mesh rings as bearing dampers at cryogenic temperatures was also investigated in this research. Three types of metal mesh, made of two different materials (copper and steel) at different densities were tested for dependency on interference and temperature. The outcome of this research shows several advantages of metal mesh bearing dampers. Some of the benefits of using metal mesh as a bearing damper follow:

1) Metal mesh dampers have low support stiffness combined with significant damping at cryogenic temperatures.

2) The significant amount of damping provided by metal mesh requires no lubrication, cooling, or auxiliary systems.

3) Metal mesh dampers are low in cost, low in maintenance, and are easily assembled/disassembled.

4) Design flexibility and control of metal mesh element stiffness and damping is obtained through a wide selection of material, manufacturing density, or even in-house changing of interference fit or axial compression.

Acknowledgments

The authors would like to acknowledge John Wall of Lockheed Martin Astronautics for significant technical contributions to the squirrel cage designs. Great appreciation is also expressed to Brent Schmidt for aiding in the data collection and test rig construction.

References

[1]Zarzour, M., and Vance, J. M., "Experimental Evaluation of a Metal Mesh Bearing Damper," *Journal of Engineering for Gas Turbines and Power*, Vol. 122, No. 2, 2000, pp. 326–329.

[2]Al-Khateeb, E., and Vance, J. M., "Experimental Evaluation of a Metal Mesh Damper In Parallel with a Structural Support," ASME Paper 2001-GT-0247, June 2001.

[3]Childs, D. W., "Space Shuttle Main Engine High-Pressure Fuel Turbopump Rotordynamic Instability Problem," *Journal of Engineering for Power*, Vol. 100, Jan. 1978, pp. 48–57.

[4]Okayasu, A., Ohta, T., Azuma, T., Fujita, T., and Aoki, H., "Vibration Problems In The LE-7 Liquid Hydrogen Turbopump," *Proceedings of the 26th AIAA/SAE/ASME/ASEE 26th Joint Propulsion Conference*, 1990, pp. 1–5.

[5]Ertas, B. H., and Vance, J. M., "The Effect of Static and Dynamic Misalignment on Ball Bearing Radial Stiffness," AIAA Paper 2002-4160, July 2002.

[6]Schmidt, B., "The Experimental Determination of the Dynamic Radial Stiffness of an Angular Contact Ball Bearing," M.S. Thesis, Texas A&M Univ., Mechanical Engineering Dept., College Station, TX, May 2001.